Faculty and Researchers   Faculty and Researchers' Publications

2006

Strain-path effects on the evolution of microstructure and texture during the severe-plastic deformation of aluminum

Salem, A.A.; Langdon, T.G.; McNelley, T.R.; Kalidindi, S.R.; Semlatin, S.L.

Springer

Strain-Path Effects on the Evolution of Microstructure and Texture during the Severe-Plastic Deformation of Aluminum

A.A. SALEM, T.G. LANGDON, T.R. McNELLEY, S.R. KALIDINDI, and S.L. SEMIATIN

Microstructure and texture evolution during the severe-plastic deformation (SPD) of unalloyed aluminum were investigated to establish the effect of processing route and purity level on grain refinement and subgrain formation. Two lots of aluminum with different purity levels (99.998 pct Al and 99 pct Al) were subjected to large plastic strains at room temperature *via* four different deformation processes: equal-channel angular extrusion (ECAE), sheet rolling, conventional conical-die extrusion, and uniaxial compression. Following deformation, microstructures and textures were determined using orientation-imaging microscopy. In commercial-purity aluminum, the various deformation routes yielded an ultrafine microstructure with a ~1.5-μm grain size, deduced to have been formed *via* a dynamic-recovery mechanism. For high-purity aluminum, on the other hand, the minimum grain size produced after the various routes was ~20 μm; the high fraction of high-angle grain boundaries (HAGBs) and the absence of subgrains/deformation bands in the final microstructure suggested the occurrence of discontinuous static recrystallization following the large plastic deformation at room temperature. The microstructure differences were underscored by the mechanical properties following four ECAE passes. The yield strength of commercial-purity aluminum quadrupled, whereas the high-purity aluminum showed only a minor increase relative to the annealed condition.

I. INTRODUCTION

THE high strength and enhanced superplastic properties associated with ultrafine microstructures in metallic alloys provide substantial benefits for a wide range of aerospace applications. Typically, grain refinement is achieved *via* large plastic strains in conventional metal-forming processes (*e.g.,* extrusion and rolling). The products of such techniques have limited structural applications, however, due to the substantial change in billet dimensions associated with the processes. On the other hand, the production of ultrafine grain structures in bulk materials has recently been facilitated by the development of novel deformation techniques such as equal-channel angular extrusion (ECAE) in which ultra-high plastic strains (*i.e.,* $\varepsilon > 5$) are imposed without a change in workpiece dimensions.[1–5]

A fine-grain microstructure can be produced *via* one of two means. So-called *discontinuous* recrystallization involves the nucleation and growth of strain-free grains, a process driven by stored dislocations acting on high mobility boundaries. The misorientations across the new grain boundaries are usually high. This process may occur during hot deformation (*i.e.,* dynamic recrystallization) or during heat treatment following cold or hot deformation (*i.e.,* classical static recrystallization). On the other hand, a micro-structure containing high-angle grain boundaries (HAGBs) may evolve continuously *during* large plastic deformation under cold- or warm-working conditions producing an ultra-fine-grained material *via* a process sometimes known as continuous recrystallization.[6,7]

The effectiveness of different deformation processes on grain refinement and subsequent mechanical behavior has been the focus of many investigations. Even for a given process (*e.g.,* ECAE), the effect of deformation route on microstructure evolution is still not totally clear. For example, the experimental studies on the ECAE of pure Al using a 90 deg die revealed that route B_c (90 deg rotation in the same sense between passes) was more effective than route C (180 deg rotation between passes) and route A (no rotation). By contrast, experiments using a 120 deg die showed that route A was most effective with regard to grain refinement.[10] This controversy has been carefully reviewed by Zhu *et al.*[11] and investigated by Furukawa *et al.*[12] Nevertheless, Hansen, *et al.*[13] have surmised that the underlying mechanism for structure refinement is *not* strongly affected by the deformation process. This latter work used TEM techniques to compare microstructure evolution during both severe-plastic and conventional deformation processes, namely, accumulative roll bonding, high-pressure torsion, rolling, and torsion. However, the data that were analyzed were extracted from different materials (aluminum, nickel, and copper) that had been processed under different deformation conditions, thereby making the interpretation of the results more difficult.

The present work was undertaken to establish the effect of straining mode on grain subdivision and texture evolution during the severe-plastic deformation of carefully controlled lots of well-characterized starting materials (commercial-purity aluminum and high-purity aluminum). To ensure a reliable comparison, the program materials were deformed *via* various means using nearly identical process variables (*i.e.,* deformation temperature, effective strain, and effective strain rate). The deformed microstructures

A.A. SALEM, Visiting Scientist, Air Force Research Laboratory, Materials and Manufacturing Directorate, AFRL/MLLM, is with Universal Technology Corp., Dayton, OH 45432. Contact e-mail: ayman.salem@wpafb.af.mil T.G. LANGDON, Professor, is with the Departments of Aerospace & Mechanical Engineering and Materials Science, University of Southern California, Los Angeles, CA 90089. T.R. McNELLEY, Professor, is with the Department of Mechanical Engineering, Naval Postgraduate School, Monterey, CA 93943. S.R. KALIDINDI, Professor and Department Head, is with the Department of Materials Science and Engineering, Drexel University, Philadelphia, PA 19104. S.L. SEMIATIN, Senior Scientist, Materials Processing/Processing Science, is with the Air Force Research Laboratory, Materials and Manufacturing Directorate, AFRL/MLLM, Wright-Patterson AFB, OH 45433.

were characterized by orientation-imaging microscopy (OIM) using a high-resolution electron-backscatter diffraction (EBSD) technique integrated with a field-emission gun–scanning electron microscope (FEGSEM). Compared to transmission electron microscopy (TEM) techniques, the high-resolution EBSD has the advantage of rapidly gathering large amounts of quantitative data over larger areas while maintaining the ability to characterize cell and subgrain boundaries except those cases characterized by very low misorientation.[14]

II. MATERIALS AND PROCEDURES

A. Materials

The effect of deformation mode on grain subdivision was revealed *via* the large-strain deformation of aluminum of two purity levels: (1) high-purity (99.998 pct Al) and (2) commercial-purity AA1100-H112 (99 pct Al). The chemical composition (in wt ppm) for the high-purity aluminum was <1 Fe, 3.5 Si, and <1 Cu and for the commercial-purity was 5800 Fe, 2000 Si, and 600 Cu.

The *high-purity* aluminum was received as a cast ingot with a coarse columnar microstructure that was broken down *via* sequential room-temperature forging along three orthogonal directions and intermediate and final annealing at 400 °C, thus yielding an equiaxed structure with an average grain size of 90 μm. The *commercial-purity* aluminum, received as 50-mm-thick cold-rolled plate, was annealed at 345 °C for 1 hour and then water quenched, thus yielding a microstructure with an average grain size of 290 μm. Orientation-imaging microscopy showed that both materials exhibited a cubelike texture with a high fraction of HAGBs (Figure 1).

B. Thermomechanical Processes

Preforms machined from the annealed materials were deformed using four different deformation methods: ECAE, sheet rolling, conical-die extrusion, and uniaxial compression. Each of the processes was conducted at room temperature using deformation speeds chosen to impart an effective strain rate of 2 s^{-1}. Samples were water quenched after each deformation (or each increment of deformation as in ECAE and rolling). Immediately after the last defor-

mation pass, each sample was stored at –70 °C to minimize static recovery and recrystallization prior to metallographic and texture examination.

1. Equal-channel angular extrusion

The ECAE trials used multipart tooling with a fixed housing and several sliding components to reduce frictional effects.[15] The equal cross-section square channels (50.8 × 50.8 mm) had an inclined angle of 90 deg. To conserve the high-purity aluminum program material, square preforms (measuring 19 × 19 mm and 108-mm length) were machined and assembled into rectangular cans (50.8 × 50.8 mm and 203-mm length) that were machined from the annealed commercial-purity aluminum plate without any parting agent between the can and the preform. Billets were given four passes through the ECAE die at a constant ram speed of 50.8 mm/s. Surface grinding was used after each pass to reduce the cross section slightly in order to facilitate subsequent insertion in the die. Each sample was rotated either 90 or 180 deg about its axis between passes; *i.e.,* route B$_c$ or route C was used. After the fourth pass, samples were sectioned longitudinally along the midplane containing the extrusion direction (ED), which was aligned with the exit channel, and the transverse direction (TD), which was aligned with the inlet channel (Figure 2). All microstructural observations were reported in the flow plane (defined by the ED and TD directions). The direction perpendicular to the flow plane is referred to as the normal direction (ND) (+Y in the previous work of Iwahashi *et al.*[16,17]).

2. Rolling

Rectangular billets measuring 12.7-mm thick × 75-mm wide × 54-mm long were employed for rolling trials. Samples were rolled at a speed of 4.76 m/min to a total reduction of 69 pct (von Mises effective strain ε_{VM} = 1.35) or 95 pct (ε_{VM} = 3.45) in 11 or 29 passes, respectively. Microstructure and OIM observations were taken on longitudinal sections that were contained the rolling direction (RD) and ND.

3. Conventional conical-die extrusion

A 700-ton press was used to conduct conventional conical-die extrusion trials on cylindrical billets measuring 31.8-mm diameter × 55.6-mm length. To obtain the desired strain rate, ram speeds of 9.7 and 3 mm/s were used for

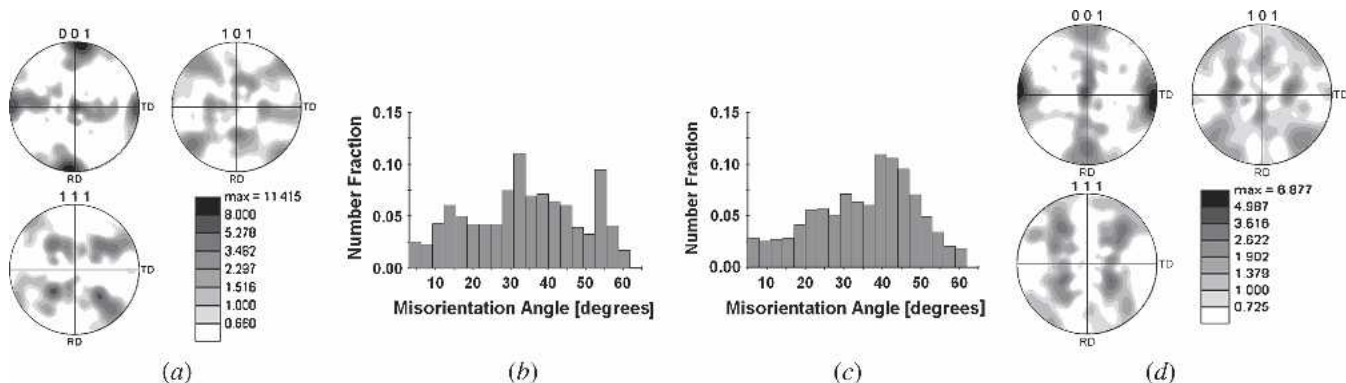Fig. 1—Pole figures and misorientation distributions for annealed program materials: (*a*) and (*b*) high-purity aluminum and (*c*) and (*d*) commercial-purity aluminum.

extrusion ratios of 3:1 ($\varepsilon_{VM} = 1.1$) and 30:1 ($\varepsilon_{VM} = 3.4$), respectively. Metallographic observations were taken along the longitudinal midplane containing the ED.

4. *Uniaxial compression*

Isothermal, constant-strain-rate, uniaxial-compression tests were conducted on cylindrical samples (10-mm diameter × 15-mm length) to an average height strain of 1.65. Molydisulfide (MoS_2) was used as a lubricant to reduce frictional effects. Load-displacement data were corrected for the compliance of the testing machine and reduced to true stress–true strain curves using standard procedures. The maximum scatter in the flow stress data from duplicate tests was less than 5 pct at any given strain. Deformed samples were sectioned axially (*i.e.,* parallel to the compression direction) for microstructure examination.

To establish the effect of SPD processing on subsequent mechanical behavior, additional compression tests were conducted on cylindrical specimens that had been cut from ECA-extruded workpieces after four passes *via* routes B_c and C. The compression axes of these samples were aligned with either the ED or ND directions of the extrudates (Figure 2).

C. *Metallography*

To quantify the evolution of microstructure and texture, deformed samples were sectioned and prepared for OIM *via* EBSD. During the sectioning and grinding operations, each sample was cooled with chilled water (at $\sim$0 °C) to minimize static recovery and recrystallization. Following grinding (using silicon carbide papers down to 1200 grit), electropolishing was performed using a potential of 25 V DC in a solution of 60 mL perchloric acid and 590 mL methanol at –20 °C. The OIM was conducted on a Leica (Bannockburn, IL) FEG/SEM using an accelerating voltage of 20 kV and a beam current of 10 nA. Kikuchi patterns were indexed using computer-based EBSD software from TexSEM Laboratories (Provo, UT). The use of FEGSEM/EBSD techniques enabled the simultaneous, detailed description of microstructure and texture evolution over large areas of each sample and thus a degree of characterization heretofore impossible during early research into large-strain deformation.[18,19]

III. RESULTS AND DISCUSSION

The principal results of this work pertained to the evolution of microstructure and texture in aluminum during SPD *via* various means and the interpretation of these results based on flow-curve measurements and crystal-plasticity analysis. The microstructures and textures were described using inverse-pole-figure maps in which boundaries were defined using a criterion based on a minimum misorientation θ of 2 deg. This minimum misorientation arose from the angular resolution of the OIM technique. In the figures presented subsequently, black boundaries represent HAGBs ($\theta > 15$ deg), while white boundaries represent low-angle grain boundaries (LAGBs, $\theta < 15$ deg). The results were interpreted in the context of previous work on fcc metals.[20–22]

A. *Equal-Channel Angular Extrusion*

Microstructure and texture evolution in high- and commercial-purity aluminum after four ECAE passes using routes B_c and C was quantified by inverse-pole-figure maps, pole figures, and misorientation distributions (Figures 2 through 5). For ECAE, the inverse-pole-figure maps denoted the crystallographic direction corresponding to the ED ($-$X in the previous work of Iwahashi *et al.*[16,17]). The average textures were calculated from the OIM data and represented by (001), (101), and (111) pole figures.

1. *ECAE—Route B_c*

After four passes of ECAE *via* route B_c, inverse-pole-figure maps for the *high-purity* aluminum revealed a highly irregular microstructure with an average grain size estimated as approximately 20 μm (Figure 2(a)) and pole figures showing a cube texture (Figure 3(a)). The misorientation distribution exhibited a large fraction of HAGBs and a low fraction of LAGBs (Figure 3(b)). A more detailed examination revealed the absence of subgrains or deformation bands in most of the grains, thus suggesting that the high-purity material had recrystallized *via* a *discontinuous* mechanism; this conclusion was also supported by the observed cube texture and the large fraction of HAGBs. The bulging of the boundaries of some grains and the observation of small grains along the boundaries of deformed grains or within grains (Figure 2(a)) offered further support to the discontinuous-recrystallization hypothesis.

An important question is whether the high-purity aluminum underwent discontinuous recrystallization *during* or *following* the imposed deformation. It has been long believed[23,24] that the high-stacking-fault energy of aluminum results in high rates of dynamic recovery that reduce the reservoir of stored energy required to drive discontinuous *dynamic* recrystallization, particularly for materials whose boundary mobility may be low at room temperature. The observations of Yamagata[25–29] and Ponge *et al.*[30] (*e.g.,* flow curves that exhibited oscillations and microstructures comprising grains with various degrees of dislocation substructure) suggested otherwise, however. On the other hand, Gourdet and Montheillet[7] argued that the absence of subgrains in portions of the microstructure could indicate that some new grains grew *after* deformation.

In the present work, the high purity level would favor discontinuous dynamic recrystallization by increasing grain-boundary mobility.[7,31] Furthermore, a few grains did show small intensity variations in the inverse-pole-figure maps, indicative of residual cold work. However, the negligible misorientation between adjacent points within *most* of the recrystallized grains suggested that the material did indeed undergo discontinuous *static* recrystallization. Despite this apparent uncertainty, the flow curves for the high-purity aluminum (discussed subsequently) did not suggest that discontinuous dynamic recrystallization had occurred, thus supporting the occurrence of classical static recrystallization that had not gone to full completion.

With regard to discontinuous dynamic recrystallization, it may also be conjectured that the temperature increase during ECAE may enhance the tendency for such a process.
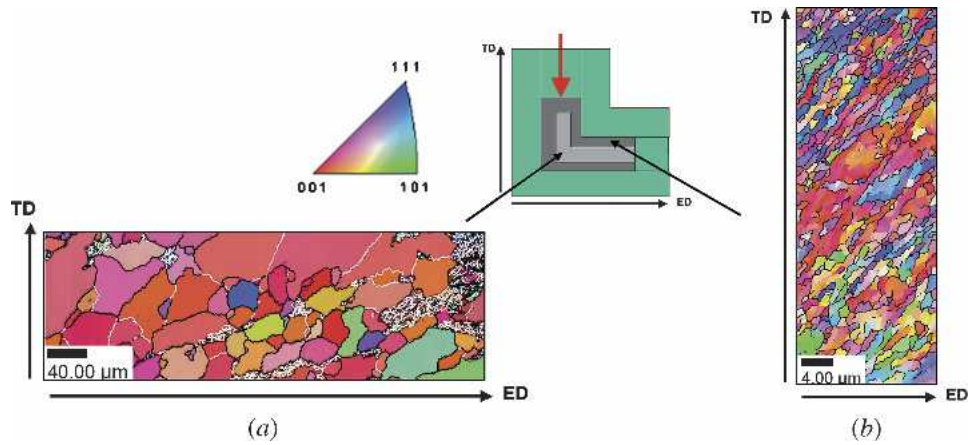
Fig. 2—Inverse-pole-figure maps for the ED after four ECAE passes (effective strain ≈ 4.6) *via* route B$_c$ for (*a*) high-purity aluminum and (*b*) commercial-purity aluminum. The ND is perpendicular to the plane of the paper.
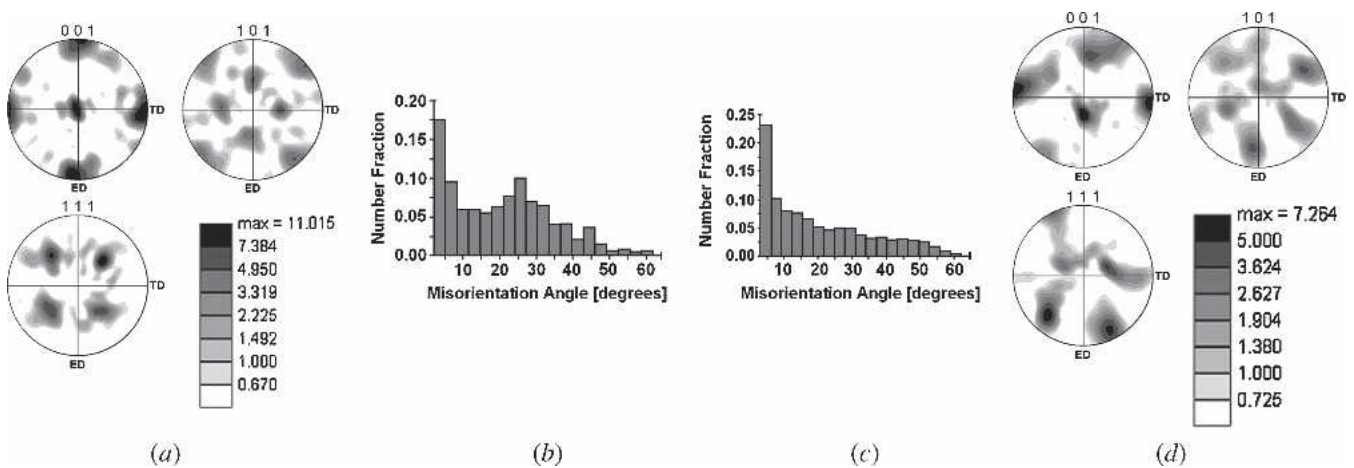

Fig. 3—Pole figures and misorientation distributions for (*a*) and (*b*) high-purity aluminum and (*c*) and (*d*) commercial-purity aluminum after four ECAE passes *via* route B$_c$.
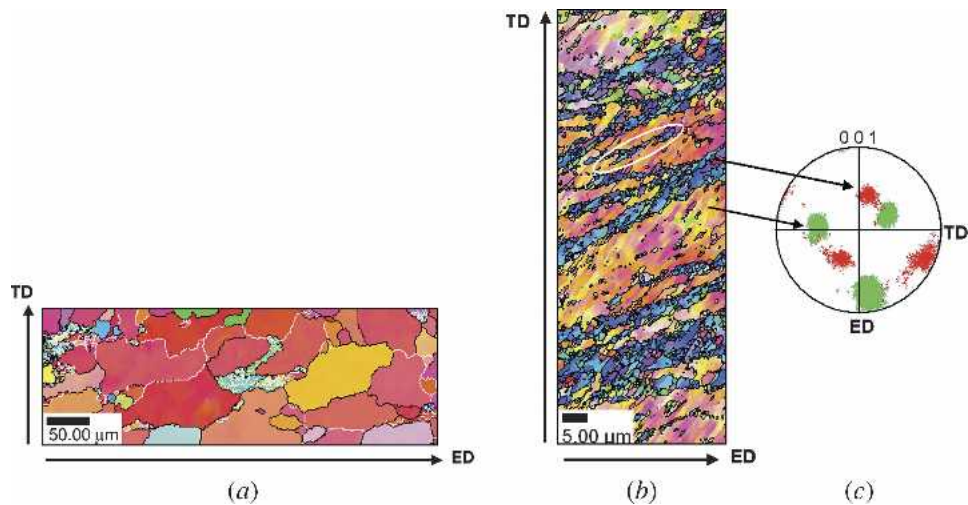

Fig. 4—Inverse-pole-figure maps for the ED after four ECAE passes (effective strain ≈ 4.6) *via* route C for (*a*) high-purity aluminum and (*b*) commercial-purity aluminum. In (*c*), the (001) pole figure for commercial-purity aluminum highlights the texture of regions with large grains (green) or small grains (red).

In this regard, Yamaguchi *et al.*[32] measured an increase in temperature of 40 °C due to deformation heating during a single ECAE pass of pure aluminum (99.99 pct Al) under ambient conditions. However, Hasegawa *et al.*[33] demonstrated that the grain size of 1.3 µm developed after four ECAE passes (route B$_c$) of high-purity aluminum (99.99 pct)
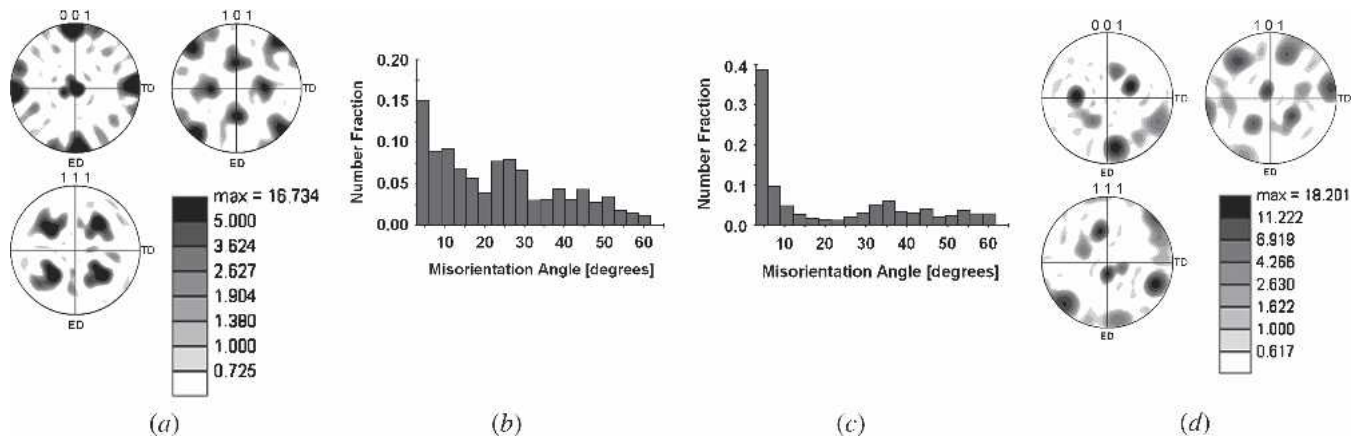
Fig. 5—Pole figures and misorientation distributions for (*a*) and (*b*) high-purity aluminum and (*c*) and (*d*) commercial-purity aluminum after four ECAE passes *via* route C.

did not change significantly during annealing at 150 °C for 1 hour.

Microstructure and texture observations for the *commercial-purity* aluminum (Figures 2(b), 3(c), and (d)) suggested that microstructure evolution for this material was controlled primarily by dynamic recovery. In contrast to the high-purity material, the commercial-purity aluminum subjected to the same deformation history (route B_c) showed an average grain size of 1.3 μm after four-pass ECAE (Figure 2(b)). Moreover, it had a smaller volume fraction of HAGBs compared to the high-purity aluminum (Figure 3(c)). These results for commercial-purity aluminum are very similar to the observations of Iwahashi *et al.*,[17] for the ECAE of *high-purity* aluminum (99.99 pct). In this former work, a grain size of 1.3 μm was most readily obtained using route B_c in tooling with a 90 deg angle at room temperature, supposedly by a dynamic recovery process. The different behaviors between the present and former lots of high-purity aluminum also suggest that rather subtle differences in purity level in the range between 99.99 and 99.998 pct may have a pronounced, but previously unrecognized, effect on boundary mobility and thus the occurrence of discontinuous recrystallization.[31]

2. *ECAE—Route C*

Four-pass ECAE *via* route C resulted in qualitatively similar microstructural features compared to those for each material processed *via* route B_c. However, the average grain sizes were larger in route C than route B_c, and the textures were stronger (Figures 4, 5(a), and (d)). In addition, the fraction of HAGBs was noticeably higher for route B_c than for route C (Figures 3(b) and (c)*vs* 5(b) and (c)). In addition, the inverse-pole-figure maps for the commercial-purity aluminum (Figure 4(b)) showed two populations of grains: large grains with similar shades of (red) color that were surrounded by small grains with another shade of color (blue). The large grains engulfed small subgrains and had the ED direction closer to <100> than the small grains, which had the ED direction closer to <111>. Parts of each large grain were separated from the rest of the grain by HAGBs that surrounded subgrains with new orientations (blue) closer to <111> (circled in Figure 4(b)). These large grains most likely evolved from the

same original grain, which was divided by subgrains that were subsequently rotated producing HAGBs. The orientations of all the big grains were separated from the rest of the grains and then plotted on a {001} pole figure (Figure 4(c)). It is clear that all the big grains belonged to one orientation (in green), and all the small grains belonged to another orientation (in red). This hypothesis supported the notion of continuous recrystallization proposed by Gourdet and Montheillet.[7]

Overall, the present results demonstrated that route B_c was more effective than route C with regard to the refinement of grain size and the development of a large fraction of HAGBs.

B. *Rolling*

The effect of thickness reduction on microstructure evolution during rolling was also well delineated in the inverse-pole-figure maps for the ND of deformed samples (Figures 6(a) through (c) and 7(a) and (d)). Misorientation measurements along different paths parallel to the RD (Figures 6(d) through (f)) quantified the heterogeneity of deformation within individual grains; black lines denote the misorientation of each grid point relative to the starting point (θ_0), and gray lines indicate the misorientation between adjacent points on the line (θ_{rel}).

For *high-purity* aluminum rolled to an effective strain of 1.35, the grains were elongated along the RD (Figures 6(a) and (b)). Orientation gradients were found in some grains (grains 1 and 2 in Figure 6(c)). However, other grains exhibited homogenous orientations (grain 3 in Figure 6(c)). After a reduction corresponding to an effective strain of 3.4, however, most of the elongated-grain structure had disappeared in the high-purity aluminum, being replaced by smaller equiaxed grains having no apparent substructure within them (Figure 7(a)).

The intensity variations within the grains in Figure 6 indicate a heterogeneity of orientation and, hence, suggest the development of subgrains in high-purity aluminum after an effective strain of 1.35. The misorientation distribution (Figure 6(g)) showed a large fraction (0.82) of low-angle boundaries and a small fraction (0.18) of HAGBs. Detailed misorientation measurements along different paths parallel
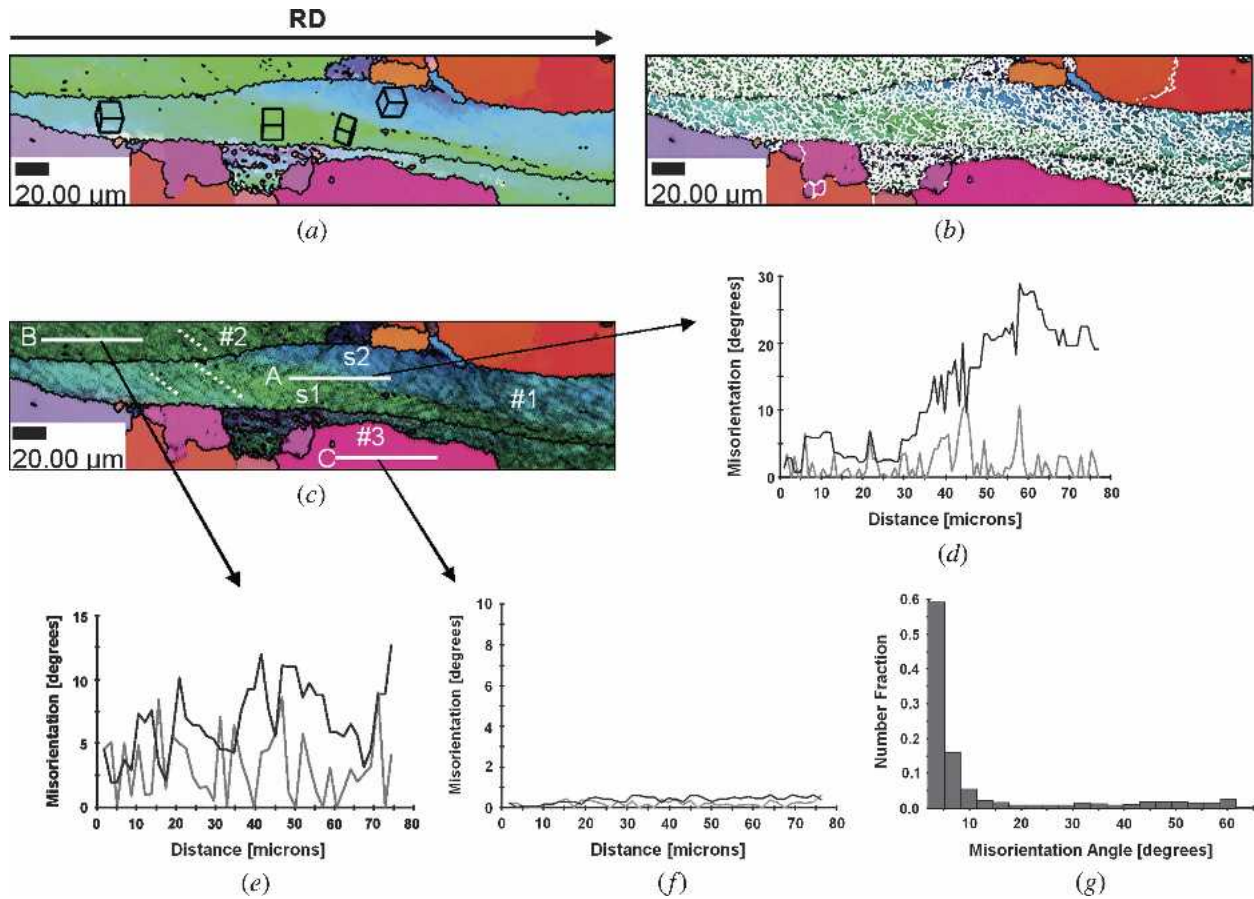
Fig. 6—(*a*) through (*c*) Inverse-pole-figure maps for the ND, (*d*) through (*f*) misorientation traverses, and (*g*) misorientation distribution for high-purity aluminum after rolling to an effective strain of 1.35. On the inverse-pole-figure maps, low-angle boundaries are white and high-angle boundaries are black. On misorientation distribution charts, black lines denote the misorientation of each grid point relative to the starting point (θ_0), and gray lines indicate the misorientation between adjacent points on the line (θ_{rel}).
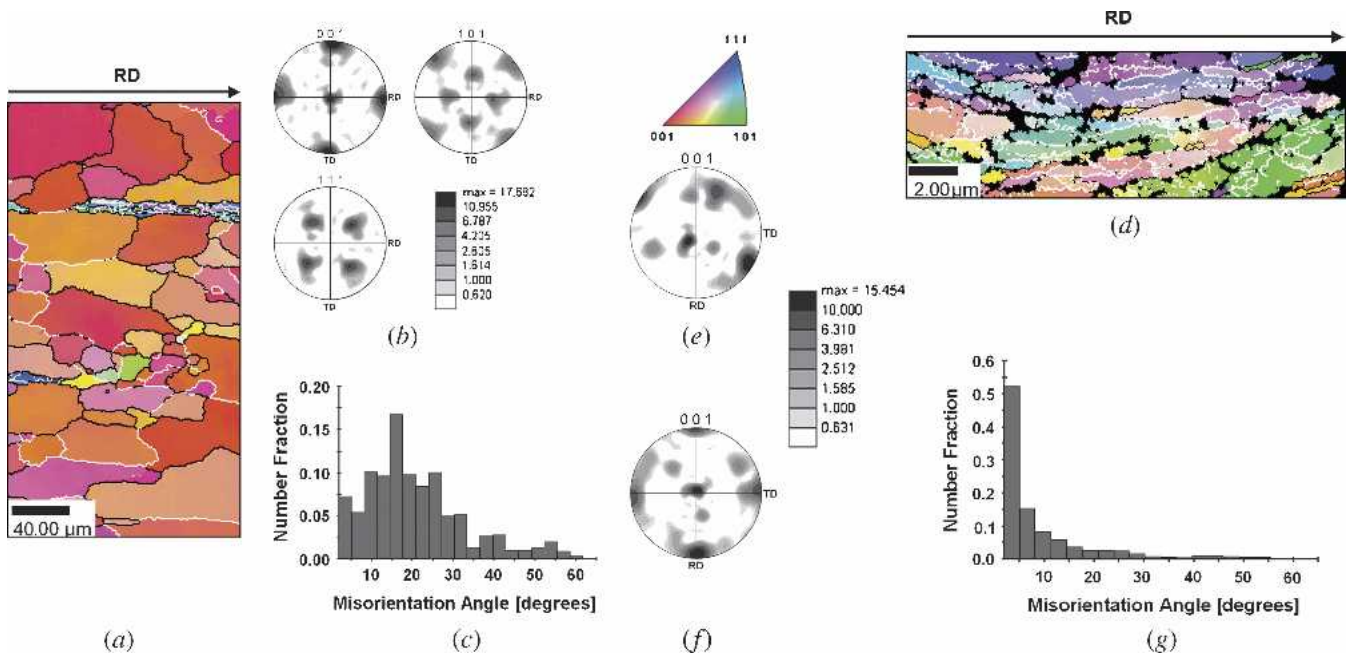

Fig. 7—Inverse-pole-figure maps for the ND, pole figures, and misorientation distributions for (*a*) through (*c*) high-purity aluminum and (*d*) through (*g*) commercial-purity aluminum after rolling to an effective strain of 3.4. On the inverse-pole-figure maps, low-angle boundaries are white, and high-angle boundaries are black: (e) as deformed and (f) after –60 deg rotation about ND followed by –20 deg rotation about RD.

to RD provided further insight into the heterogeneity of deformation (Figures 6(d) through (f)). Along path A, a sudden increase in θ_0 was observed for the right half of the grain ($\theta_0 > 10$ deg with an average value of 19.8 deg and a maximum of 29 deg) compared to the left half ($\theta_0 < 10$ deg with an average value of 4 deg and a maximum of 9.7 deg) (Figure 6(d)). This increase underscored the transition from one band (S1) to another (S2) with an average θ_{rel} of 1.2 deg within the lower band (S1) and 2.6 deg within the upper band (S2). In grain 2, similar measurements along path B showed a noticeable variation in both θ_0 and θ_{rel} along the entire length with maximum values of 12 and 9 deg and average values of 6 and 3 deg, respectively (Figure 6(e)). On the other hand, misorientation measurements along path C inside grain 3, with no apparent orientation gradients, showed changes in θ_{rel} and θ_0 less than the resolution of the EBSD system (Figure 6(f)).

Changes in intensity (from light green in the bottom to dark blue in the top) within grain 1 of the high-purity aluminum sample rolled to the lower reduction (Figure 6(a)) suggested grain subdivision by the formation of high-angle boundaries and the development of bandlike regions within elongated prior grains. The grayscale map of EBSD image quality shown in Figure 6(c) revealed the deformation substructure in more detail. In such maps, dark areas represent poor image quality, which may result from the interaction of the electron beam with dense arrays of dislocations. These maps revealed planar structures lying at an angle of 40 deg to the RD, as indicated by the dashed white lines in Figure 6(c). These observations are consistent with previous studies of cold-rolled commercial-purity aluminum using TEM[34] and OIM.[35]

At the higher reduction, corresponding to an effective strain of 3.4, *high-purity* aluminum exhibited a structure consisting primarily of slightly elongated grains with an average grain size of 40 μm and a strong cube texture (Figures 7(a) through (c)). No deformation bands were observed. The misorientation distribution (Figure 7(c)) showed a large fraction (0.70) of HAGBs and a small fraction (0.3) of LAGBs. Detailed measurements of misorientation profiles showed that most of the grains had negligible values of θ_0 and θ_{rel}, *i.e.*, values less than the resolution of the EBSD/FEGSEM system. Thus, as for four-pass ECAE involving a comparable strain level, it may be concluded that the high-purity aluminum underwent discontinuous static recrystallization.

The microstructure of the *commercial-purity* aluminum cold rolled to an effective strain of 3.4 showed an average grain size of 1 μm with a high number fraction (0.80) of LAGBs (Figures 7(d) and (g)) and a rotated cube texture with an *S* component (Figures 7(e) and (f)). These microstructure results (*i.e.,* grain size) are similar in nature to those for four-pass ECAE of this material (Figures 2(b) and 4(b)). The high fraction of LAGBs is similar to the observations for ECAE *via* route C (Figure 5(c)), but is in contrast to the large fraction of HAGBs for ECAE *via* route B$_c$ (Figure 3(c)).

C. *Conventional Conical-Die Extrusion*

The evolution of microstructure in *high-purity* aluminum during cold extrusion to area reductions corresponding to

an effective strain of 1.1 or 3.4 was also well described by inverse-pole-figure maps. At an effective strain of 1.1, the original grains (defined by high-angle boundaries) were elongated parallel to the ED and appeared to have been subdivided into subgrains and bandlike regions, as indicated by intensity variations (Figure 8(a)). Specifically, HAGBs were observed within the middle grain separating the area on the top from the rest of the grain. The misorientation profile across this region revealed a sudden change in θ_0 (from 6 to 30 deg) at the boundary between the bandlike area on the top and the rest of the grain (Figure 8(b)). In addition, the misorientation distribution confirmed that a high fraction (0.77) of LAGBs (Figures 8(a) and (c)) developed within the microstructure.

Intensity variations within the grains almost disappeared upon further deformation of the high-purity aluminum *via* conical-die extrusion to an effective strain of 3.4 (Figure 8(d)), similar to the observations in both ECAE and rolling to comparable strain levels. At this deformation level, an equiaxed microstructure with an average grain size of ~20 μm (Figure 8(d)) and a cubelike texture (Figure 8(e)) similar to the initial texture of the starting (annealed) material were developed. Furthermore, the misorientation distribution (Figure 8(f)) revealed a high fraction (0.75) of HAGBs.

Similar to the observations in rolling, the *commercial-purity* aluminum showed elongated grains along the ED direction with intense substructure formation within the grains at a strain of 1.1. In quantitative terms, the microstructure comprised a large fraction of LAGBs (0.6). Unfortunately, extrusion of the commercial-purity aluminum to an effective strain of 3.4 was not possible because of press limitations.

D. *Uniaxial Compression*

The microstructures developed after a true strain of 1.65 in uniaxial compression were very similar to those previously described for ECAE, rolling, and conical-die extrusion. Inverse-pole-figure maps for the compression direction for both high-purity and commercial-purity aluminum revealed the subdivision of grains into subgrains (Figures 9(a) and (c)). Almost all of the initial grains were elongated in the direction perpendicular to the loading direction. Misorientation distributions showed a high fraction of LAGBs in both materials (Figures 9(b) and (d)), which were also evident in the inverse-pole-figure maps as white boundaries (Figures 9(a) and (c)).

A noticeable heterogeneity of deformation on a large scale was also noted for the high-purity aluminum deformed to a strain of 1.65. Grains with a <101> direction close to the compression axis showed the most noticeable grain subdivision, as indicated by the LAGBs. In contrast, grains with a <001> direction close to the loading direction showed a very small number of subgrains and in many cases no subgrains at all (Figure 9(a)). Evidence of the incidence of boundary migration and discontinuous recrystallization was also found in parts of the microstructure of the high-purity aluminum sample (*e.g.,* the middle grain in Figure 9(a)).

The average grain sizes developed during compression to a true strain of 1.65 were very similar to those developed *via* the other deformation modes, *i.e.,* ~40 μm in high-purity
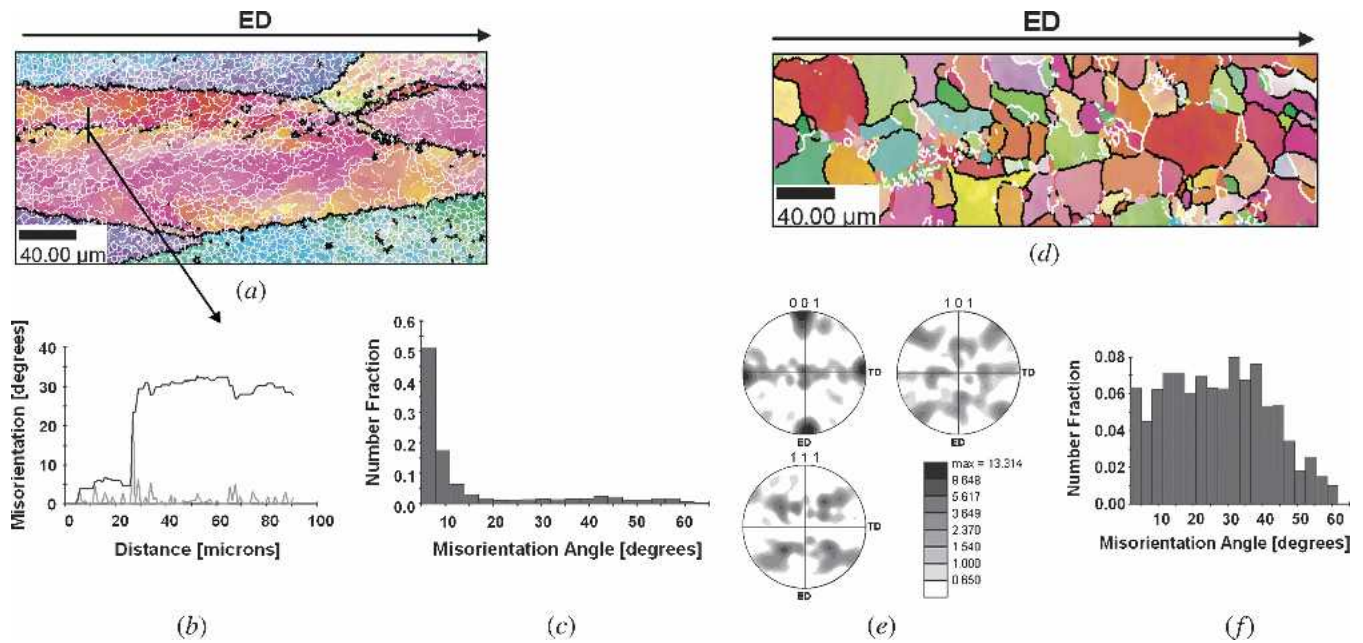
Fig. 8—Inverse-pole-figure maps for the radial direction, misorientation distributions, and pole figures for high-purity aluminum deformed *via* conical-die extrusion to an effective strain of (*a*) through (*c*) 1.1 or (*d*) through (*f*) 3.3. On the inverse-pole-figure maps, low-angle boundaries are white, and high-angle boundaries are black.
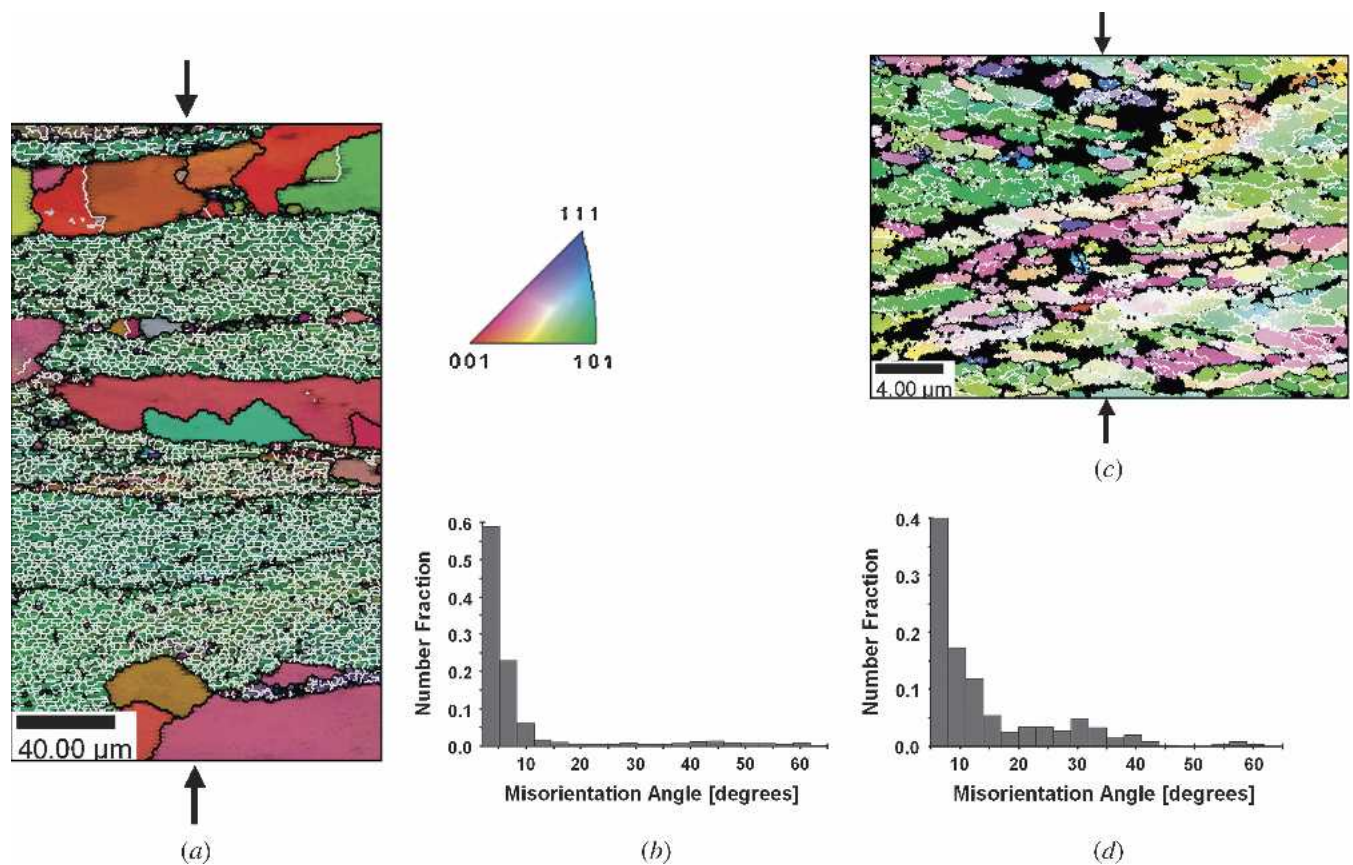

Fig. 9—Inverse-pole-figure maps for the compression-axis direction and misorientation distributions for (*a*) and (*b*) high-purity aluminum and (*c*) and (*d*) commercial-purity aluminum after an effective strain of 1.65 in simple compression. On the inverse-pole-figure maps, low-angle boundaries are white, and high-angle boundaries are black.

aluminum and 1.2 μm in the commercial-purity aluminum. Such an effect of purity level on microstructure development is even more striking in light of the fact that the initial grain size of the commercial-purity aluminum was almost 3 times the initial grain size of the high-purity aluminum prior to SPD.

E. *Flow Behavior*

The flow behavior of the program materials both *prior to* SPD and *following* ECAE provided additional insight into the mechanisms of deformation and microstructure evolution of the high-purity- and commercial-purity-aluminum program materials.

3. *Flow behavior prior to SPD*

The flow behavior of the two different lots of aluminum prior to SPD showed a number of similarities and some differences. Following yielding, both materials exhibited strain hardening to the maximum strains used in the compression tests (*i.e.,* ~1.65) (Figure 10). Such stress-strain curves are indicative of flow controlled by the competition between dislocation multiplication and the annihilation of dislocations by dynamic recovery processes. Hence, it may be concluded that discontinuous *dynamic* recrystallization, for which a flow stress maximum is usually observed, did *not* occur, at least for the strain levels imposed in the present compression tests. A comparison of the flow curves for the two lots of material also revealed a lower yield strength and a lower strain-hardening rate in the high-purity aluminum compared to the commercial-purity aluminum (Figure 10). Furthermore, the starting texture did not appear to have a significant impact on the stress-strain behavior of the commercial-purity aluminum, procured as a rolled plate material, as shown by the similarity in the flow behavior along three orthogonal directions (RD, TD, and ND).

The dislocation multiplication and dynamic recovery processes controlling the shape of the flow curves were quantified using a state-variable model. Such models are usually based on a single state variable (*e.g.,* the overall dislocation density)[36–39] or several state variables related to the density and type of dislocations.[40–47] In the present work, the one-parameter model based on dislocation density developed by Yoshie *et al.*[48] and expanded upon by

Laasraoui and Jonas[49] was employed. The model is based on the assumption that dynamic recovery is the only softening mechanism, for reasons mentioned previously. The evolution of dislocation density (ρ) with strain ε is assumed to depend on the competition between strain hardening and dynamic recovery as follows:

$$d\rho/d\varepsilon = d\rho/d\varepsilon_{storage} - d\rho/d\varepsilon_{recovery} = U - \Omega\rho \quad [1]$$

in which U denotes the rate of dislocation generation due to strain hardening and Ω is the rate of dynamic recovery. Assuming that U is independent of strain, it may be shown that the flow stress σ and the steady-state (saturation) stress σ_{ss} are given as follows:

$$\sigma = [\sigma_{ss}^2 + (\sigma_o^2 - \sigma_{ss}^2)e^{-\Omega\varepsilon}]^{0.5} \quad [2a]$$

$$\sigma_{ss} = \alpha G \mathbf{b}(U/\Omega)^{0.5} \quad [2b]$$

Equation [2] was fit to the stress-strain data for both the high- and commercial-purity aluminum materials over the range of experimental conditions; U and Ω were determined using a least-squares best-fit method[50] (Figure 11). The values of U so determined were 7.3×10^{16}/m² and 4.6×10^{16}/m² for commercial- and high-purity aluminum, respectively. Furthermore, Ω was found to be 1.33 for commercial-purity aluminum and 1.58 for high-purity aluminum. A comparison of these material coefficients indicates not unexpectedly that impurities led to higher rates of dislocation multiplication and lower rates of recovery due to more barriers to dislocation motion and the increased difficulty of climb/cross-slip, respectively. However, the overall differences in the material coefficients are not large. A more important conclusion can be reached based on an extrapolation of the stress-strain behavior to strain levels comparable to those used in the SPD processes (*i.e.,* $\varepsilon \sim 3$ to 3.5), as shown in Figure 11. This extrapolation reveals that the flow stress did *not* saturate at the strain levels used in this work, and thus dynamic recovery most likely controlled deformation and microstructure evolution at high strains as well. The predictions of the current work (*i.e.,* stress saturation of 123 MPa at $\varepsilon > 3.5$) are in excellent
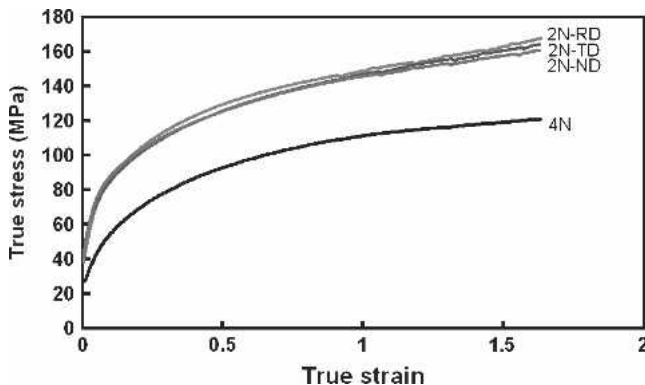

Fig. 10—Comparison of the compression flow curves for high-purity aluminum (4N) and commercial-purity aluminum (2N), the latter tested along three orthogonal directions.
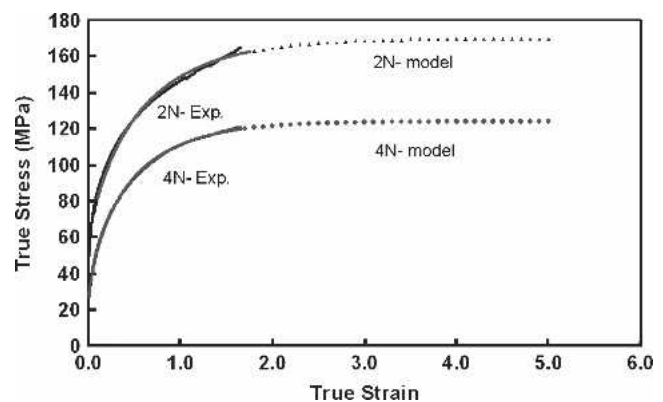

Fig. 11—Comparison of measured and fitted stress-strain curves for high- and commercial-purity aluminum (4N and 2N, respectively).

agreement with the observations of flow stress saturation by Chinh *et al.*,[51] during ECAE of high-purity aluminum. Particularly, they documented that the 0.2 pct proof stress saturated at ~120 MPa upon applying strains higher than four.

4. *Flow behavior after SPD*

The significant difference in microstructure observed following SPD of high-purity and commercial-purity aluminum was also mirrored in the post-SPD room-temperature flow curves measured on compression samples extracted from four-pass ECAE workpieces (Figures 12 and 13). For the high-purity aluminum, four-pass ECAE did not have a major impact on the stress-strain behavior compared to the annealed material (Figure 12); only a minor increase in yield strength was found. This comparison confirmed that the majority of the dislocation substructure had been eliminated due to discontinuous recrystallization.

In contrast to the behavior for the high-purity material, ECAE processing had a very large effect on both the yield strength and the strain-hardening behavior of commercial-purity aluminum (Figure 13). The material exhibited a four-

fold increase in the yield strength and a rapid saturation in strain hardening that led to a pronounced peak at small strains (less than 0.1). Moreover, the flow curves showed a greater dependence on test direction (ED *vs* ND) after route C compared to route B$_c$ (Figures 13(a) *vs* (b)). However, such directionality was still relatively small (~10.6 pct maximum difference in the peak strength) and dissipated by modest strain levels.

The observation of a marked peak stress at low strains has been noted previously in materials with ultrafine grains, as in the recent reports by Wang and Ma.[51] These authors suggested that such peaks in stress-strain curves were due to discontinuous dynamic recrystallization. Although their suggestion may be true for a very high-purity material, it is unlikely for the present commercial-purity aluminum, which exhibited no signs of new, strain-free grains even after four passes of ECAE (Figure 4(b)). Rather, the observed flow-stress saturation and subsequent softening can be hypothesized to be a result of a substructure instability or texture softening associated with the change in the deformation path (simple shear to uniaxial compression). Such a change in deformation path was proven to have a
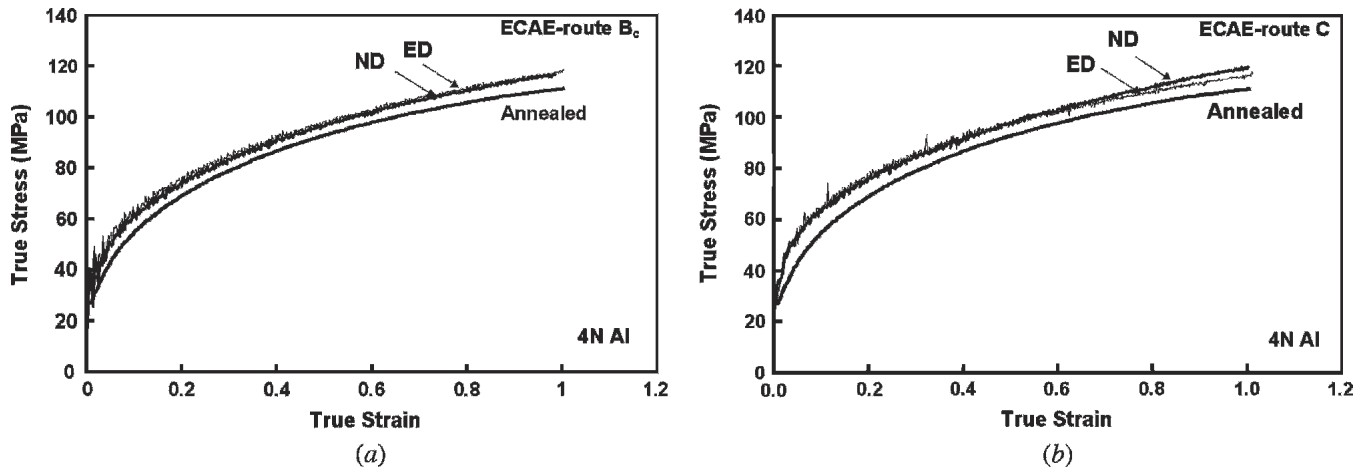
Fig. 12—Comparison of the stress-strain behavior of high-purity aluminum (4N Al) in the annealed condition and after four-pass ECAE *via* (*a*) route B$_c$ or (*b*) route C.
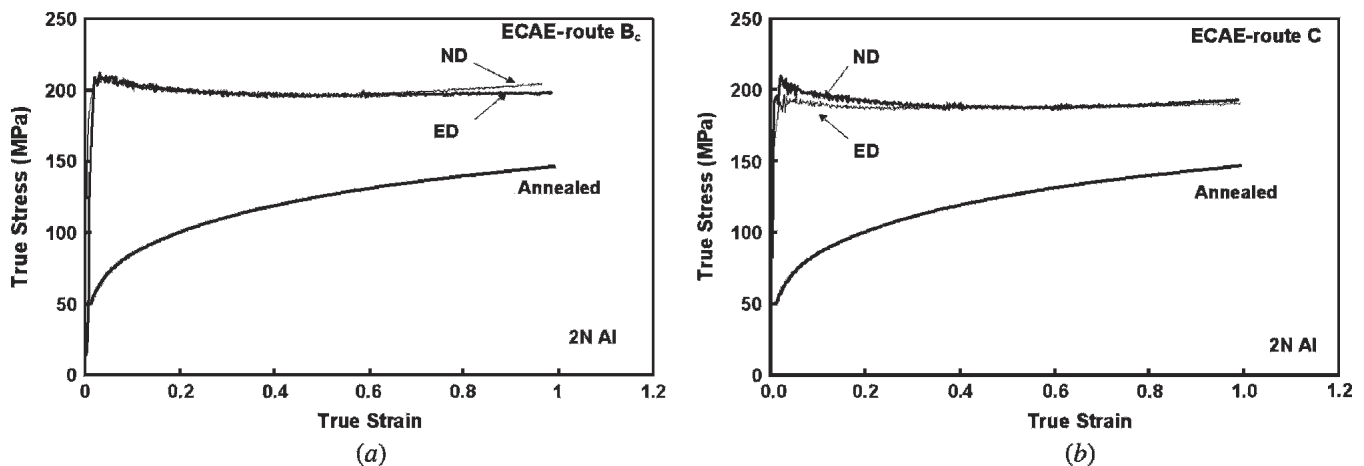
Fig. 13—Comparison of the stress-strain behavior of commercial-purity aluminum (2N Al) in the annealed condition and after four-pass ECAE *via* (*a*) route B$_c$ or (*b*) route C.

significant impact on the flow stress as well as the strain hardening behavior of other cubic metals.[53]

F. Slip-System Activity

The quantitative microstructure information discussed in Sections A through D and particularly the measured misorientation distributions suggest a considerable influence of deformation mode on the evolution of HAGBs. For a given imposed strain, different slip systems, each with varying amounts of shear, may be activated within grains of different orientations. The rate of dislocation multiplication and dynamic recovery may also vary depending on crystallographic orientation. Therefore, quantifying the activity of different slip systems might be expected to provide insight into the significant difference between the microstructure development *via* the various methods of deformation.

As a first step in the development of a complete crystal-plasticity-based model for substructure evolution during SPD, the relative activity of various slip systems was estimated for the deformation processes used in the present work. Specifically, a Taylor-type (isostrain) model[53] was used to deduce the shear strains developed for each of the 12 slip systems in fcc crystals during (a) four-pass ECAE *via* routes B_C or C and (b) deformation to an effective strain of four in uniaxial compression and plane-strain compression. The details of the model can be found elsewhere.[55,56,57] The main assumptions in this approach are that the local deformation gradient in each grain is the same as the macroscopic deformation gradient F, and that all grains have equal volume. Hence, the macroscopic Cauchy stress in the polycrystal, $\bar{T}$, can be expressed as

$$\bar{T} = \frac{1}{N} \sum_{k=1}^{N} T^{(k)} \qquad [3]$$

in which $T^{(k)}$ denotes the Cauchy stress in the kth crystal, and N is the total number of grains in the polycrystalline material. The constitutive equation for the elastic response in each grain is taken as

$$T^* = C[E^*] = F^{*-1}\{(\det F^*)T\}F^{*-T}, \quad E^* = \frac{1}{2}\{F^{*T}F^* - 1\} \qquad [4]$$

in which C denotes the fourth-order elasticity tensor, T^* and E^* are the "work-conjugate" stress and strain measures, and T is the Cauchy stress. The term F^* is the local elastic deformation gradient due to both elastic stretches and lattice rotation, which is determined by multiplicative decomposition of the local deformation gradient F (equal to the macroscopic deformation gradient), *viz*.

$$F = F^*F^p \qquad [5]$$

Here, F^p represents the local *plastic* deformation gradient due to slip such that $\det F^p = 1$ (due to plastic incompressibility). The term F^p is given by the flow rule

$$\dot{F} = L^pF^p, \quad L^p = \sum_\alpha \dot{\gamma}^\alpha S_o^\alpha, \quad \text{and} \quad S_o^\alpha = m_o^\alpha \otimes n_o^\alpha \qquad [6]$$

Here, $\dot{\gamma}$ denotes the plastic shearing rate on the α-slip system, and m_o^α and n_o^α denote the slip direction and the slip plane, respectively, in the initial unload configuration. The plastic shearing rate $\dot{\gamma}^\alpha$ on a slip system can be expressed by the power-law relationship as

$$\dot{\gamma}^\alpha = \dot{\gamma}_o \left|\frac{\tau^\alpha}{s^\alpha}\right|^{1/m} sign(\tau^\alpha), \quad \tau^\alpha \approx T^* \cdot S_o^\alpha \qquad [7]$$

in which τ^α and s^α denote the resolved shear stress on the α-slip system and the slip resistance (evolving critical resolved shear stress) of that slip system, respectively. The reference slip rate, $\dot{\gamma}_o$, was arbitrarily set as 0.001 s^{-1}, and the strain rate sensitivity parameter, m, was taken as 0.01.

Per the measured starting textures of both program materials (Figure 1), attention was focused on the deformation of an fcc single crystal with an initial cube orientation. Furthermore, it was assumed that all of the deformation was accommodated by dislocation glide/shear on {111}<110> systems; dynamic recovery (and recrystallization) and associated processes such as climb were neglected as was the latent hardening of individual slip systems. Each slip system was assigned a number from 1 to 12 to track its activity during the different deformation routes (Table I). For the ECAE simulations, a shear strain of 2.0 was imposed followed by a 90 or 180 deg rotation about the ED between passes to simulate routes B_c and C, respectively.

The results of the crystal-plasticity simulations are summarized in Figure 14 in terms of the accumulative (algebraic) sum of the shear strains for each slip system. For ECAE *via* route C, the billet is rotated 180 deg between passes and, thus, the shear on each system is reversed during alternate cycles. Therefore, the accumulated shear strain is zero after an even number of passes. This result supports the observation in Section A–2 of a low fraction of HAGBs due to the cyclic nature of straining and also is in agreement with the findings of Prangnell *et al.*[58] On the other hand, ECAE deformation *via* route B_c comprised the activation of all 12 slip systems (Figure 14), a feature which suggests why this route readily produced a high fraction of HAGBs (Section A–1). Similarly, Furukawa *et al.*[12] proved the effectiveness of route B_c by comparing constructed shear patterns of ECAE *via* routes, A, B_c, and C.

Table I.   Definition of Slip Systems Used in Crystal-Plasticity Simulations

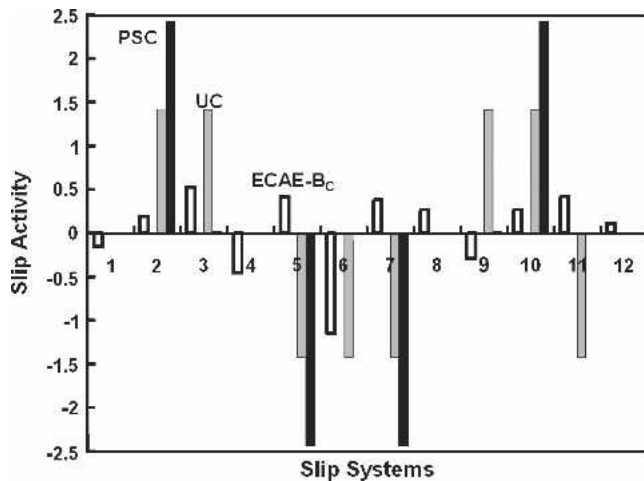| System Number	Slip Plane	Slip Direction
1	(111)	[1$\bar{1}$0]
2		[10$\bar{1}$]
3		[01$\bar{1}$]
4	($\bar{1}\bar{1}$1)	[1$\bar{1}$0]
5		[101]
6		[011]
7	($\bar{1}$11)	[101]
8		[110]
9		[01$\bar{1}$]
10	(1$\bar{1}$1)	[10$\bar{1}$]
11		[011]
12		[110]

Fig. 14—Crystal-plasticity calculations of the cumulative shear strain on each slip system in an fcc crystal with an initial cube orientation deformed to an effective strain of 4.6 *via* ECAE (routes B$_c$ and C), uniaxial compression, or plane-strain compression.

The current simulations also revealed that monotonic deformation in uniaxial compression and plane-strain compression leads to the activation of fewer slip systems (albeit larger shear per system) compared to ECAE *via* route B$_c$. In light of the observations that primarily LAGBs are formed during plane-strain deformation *via* rolling (Section B) or axisymmetric deformation *via* conical-die extrusion (Section C), it appears that a large number of activated slip systems are desirable for the formation of HAGBs.

IV. CONCLUSIONS

1. Microstructure evolution in high-purity (99.99 pct Al) and commercial-purity (99 pct Al) aluminum during severe-plastic deformation was characterized by EBSD/FEGSEM following equal-channel angular extrusion, sheet rolling, conventional (conical-die) extrusion, and simple compression. For a given deformation mode and level of imposed strain, the final grain size was much larger in the high-purity aluminum than in the commercial-purity aluminum.
2. Ultrafine grain structures were developed only in the commercial-purity aluminum; irrespective of deformation route, an average grain size of ~1.5 μm was developed in this material, apparently *via* a *continuous* dynamic-recrystallization process.
3. Large deformation of the high-purity aluminum yielded a minimum grain size of ~20 μm with a high fraction of HAGBs and cubelike textures indicating *discontinuous* recrystallization at effective strains larger than 3.
4. The flow curves of both types of aluminum suggested that deformation in both cases was controlled by dynamic recovery. Thus, the discontinuous recrystallization found for high-purity aluminum occurred most likely *following*, not during, deformation.
5. Because of the differences in the nature of the recrystallization process, the post-ECAE flow response was very different for high- and commercial-purity aluminum. The stress-strain behavior of the former material was

almost identical to that of its undeformed counterpart, whereas ECAE of commercial-purity aluminum led to significant increases in flow stress due the development of a refined microstructure with a high level of retained dislocations.
6. Crystal-plasticity analysis suggested that the activation of a large number of slip systems may be beneficial with respect to the evolution of fine microstructures with a large fraction of HAGBs.

REFERENCES

1. V.M. Segal, V.I. Reznikov, A.E. Drobyshevskiy, and V.I. Kopylov: *Russ. Metall.*, 1981, vol. 1, pp. 99-105.
2. R.Z. Valiev, N.A. Krasilnikov, and N.K. Tsenev: *Mater. Sci. Eng*, 1991, vol. A137, pp. 35-40.
3. R.Z. Valiev, A.V. Korznikov, and R.R. Mulyukov: *Mater. Sci. Eng*, 1993, vol. A168, pp. 141-48.
4. V.M. Segal: *Mater. Sci. Eng.*, 1995, vol. A197, pp. 157-64.
5. R.Z. Valiev, R.K. Islamgaliev, and I.V. Alexandrov: *Progr. Mater. Sci.*, 2000, vol. 45, pp. 103-89.
6. F.J. Humphreys, P.B. Prangnell, and R. Priestner: *Curr. Opin. Solid State Mater. Sci.*, 2001, vol. 5, pp. 15-21.
7. S. Gourdet and F. Montheillet: *Mater. Sci. Eng*, 2000, vol. A283, pp. 274-88.
8. M. Furukawa, Y. Iwahashi, Z. Horita, M. Nemoto, and T.G. Langdon: *Mater. Sci. Eng*, 1998, vol. A257, pp. 328-32.
9. K. Oh-Ishi, Z. Horita, M. Furukawa, M. Nemoto, and T.G. Langdon: *Metall. Mater. Trans. A*, 1998, vol. A29, pp. 2011-13.
10. P.B. Prangnell, A. Gholinia, and M.V. Markushev: in *Investigations and Applications of Severe Plastic Deformation*, T.C. Lowe and R.Z Valiev, eds., Kluwer Academic Publishers, Dordrecht, The Netherlands, 2000, pp. 65-71.
11. Y.T. Zhu and T.C. Lowe: *Mater. Sci. Eng.*, 2000, vol. A291, pp. 46-53.
12. M. Furukawa, Z. Horita, and T.G. Langdon: *Mater. Sci. Eng.*, 2002, vol. A332, pp. 97-109.
13. N. Hansen, X. Huang, and D.A. Hughes: in *Ultrafine Grained Materials II*, Y.T. Zhu, T.G. Langdon, R.S. Mishra, S.L. Semiatin, M.J. Saran, and T.C. Lowe, eds., TMS, Warrendale, PA, 2002, pp. 3-14.
14. P.J. Hurley and F.J. Humphreys: *Acta Mater.*, 2003, vol. 51, pp. 1087-102.
15. S.L. Semiatin and D.P. DeLo: *Mater. Des.*, 2000, vol. 21, pp. 311-22.
16. Y. Iwahashi, M. Furukawa, Z. Horita, M. Nemoto, and T.G. Langdon: *Metall. Mater. Trans. A*, 1998, vol. 29A, pp. 2245-52.
17. Y. Iwahashi, Z. Horita, M. Nemoto, and T.G. Langdon: *Acta Mater.*, 1998, vol. 46, pp. 3317-31.
18. G. Langford and M. Cohen: *Metall. Trans. A*, 1975, vol. 6A, pp. 901-10.
19. J. Gil Sevillano, P. Van Houte, and E. Aernoudt: *Progr. Mater. Sci.*, 1981, vol. 25, pp. 69-412.

20. Y. Iwahashi, Z. Horita, M. Nemoto, and T.G. Langdon: *Acta Mater.*, 1997, vol. 45, pp. 4733-41.
21. T.R. McNelley, D.L. Swisher, Z. Horita, and T.G. Langdon: in *Ultrafine Grained Materials II*, Y.T. Zhu, T.G. Langdon, R.S. Mishra, S.L. Semiatin, M.J. Saran, and T.C. Lowe, eds., TMS, Warrendale, PA, 2002, pp. 15-23.
22. S.D. Terhune, D.L. Swisher, K. Oh-Ishi, T.G. Langdon, and T.R. McNelley: *Metall. Mater. Trans. A*, 2002, vol. 33A, pp. 2173-84.
23. D. Hardwick, C.M. Sellars, and W.J. McG. Tegart: *J. Inst. Met.*, 1961–62, vol. 90 (21) pp. 21-23.
24. H.J. McQueen and K. Conrad: in *Microstructural Control in Al Alloys Processing,* H. Chin and H.J. McQueen, eds., TMS-AIME, Warrendale, PA, 1986, pp. 197-219.
25. H. Yamagata: *Scripta Metall. Mater.*, 1992, vol. 27, pp. 201-03.
26. H. Yamagata: *Scripta Metall. Mater.*, 1992, vol. 27, pp. 727-32.
27. H. Yamagata: *Scripta Metall. Mater.*, 1992, vol. 27, pp. 1157-60.
28. H. Yamagata: *Scripta Metall. Mater.*, 1992, vol. 30, pp. 411-16.
29. H. Yamagata: *Acta Metall. Mater.*, 1995, vol. 43, pp. 723-29.
30. D. Ponge, M. Bredehoft, and G. Gottstein: *Scripta Metall. Mater.*, 1997, vol. 37, pp. 1769-75.
31. C. Chovet, S. Gourdet, and F. Montheillet: *Proc. Int. Conf. UHPM 98*, Sevrier Annecy Lake, France, 1998, pp. 67-74.
32. D. Yamaguchi, Z. Horita, M. Nemoto, and T.G. Langdon: *Scripta Mater.*, 1999, vol. 41, pp. 791-96.
33. H. Hasegawa, S. Komura, A. Utsunomiya, Z. Horita, M. Furukawa, M. Nemoto, and T.G. Langdon: *Mater. Sci. Eng. A.*, 1999, vol. A265, pp. 188-96.
34. Q. Liu, X. Huang, D.J. Lloyd, and N. Hansen: *Acta Mater.*, 2002, vol. 50, pp. 3789-802.
35. L. Delannay, O.V. Mishin, D. Juul Jensen, and P. Van Houtte: *Acta Mater.*, 2001, vol. 49, pp. 2441-51.
36. U.F. Kocks: *J. Eng. Mater. Technol.*, 1976, vol. 98, pp. 76-85.
37. H. Mecking and U.F. Kocks: *Acta Metall. Mater.*, 1981, vol. 29, pp. 1865-75.
38. Y. Estrin and H. Mecking: *Acta Metall. Mater.*, 1984, vol. 32, pp. 57-70.
39. G. Gottstein and A.S. Argon: *Acta Metall. Mater.*, 1987, vol. 35, pp. 1261-71.
40. H. Mughrabi: *Acta Metall. Mater.*, 1983, vol. 31, pp. 1367-79.
41. F.B. Prinz: *Acta Metall. Mater.*, 1984, vol. 32, pp. 1021-28.
42. H. Mughrabi: *Mater. Sci. Eng.*, 1987, vol. 85, pp. 15-31.
43. M. Zehetbauer and V. Seumer: *Acta Metall. Mater.*, 1993, vol. 41, pp. 577-88.
44. M. Zehetbauer: *Acta Metall. Mater.*, 1993, vol. 41, pp. 589-99.
45. A.S. Argon and P. Haasen: *Acta Metall. Mater.*, 1993, vol. 41, pp. 3289-306.
46. Y. Estrin, L.S. Toth, A. Molinari, and Y. Brechet: *Acta Mater.*, 1998, vol. 46, pp. 5509-22.
47. M. Goeordeler and G. Gottstein: *Mater. Sci. Eng. A*, 2001, vols. A309–A310, pp. 377-81.
48. A. Yoshie, H. Morikawa, and Y. Onoe: *Trans. Iron Steel Inst. Jpn.*, 1987, vol. 27, pp. 425-31.
49. A. Laasraoui and J.J. Jonas: *Metall. Trans A*, 1991, vol. 22A, pp. 1545-58.
50. W.H. Press, S.A. Teukolsky, W.T. Vetterling, and B.P. Flannery: *Numerical Recipes in Fortran 77*, Cambridge University Press, New York, NY, 1992, pp. 678-83.
51. N.Q. Chinh, G. Horvath, Z. Horita, and T.G. Langdon: *Acta Mater.*, 2004, vol. 52, pp. 3555-63.
52. Y.M. Wang and E. Ma: *Mater. Sci. Eng.,* 2004, vols. A375–A377**,** pp. 46-52.
53. B. Peeters, M. Seefeldt, C. Teodosiu, S.R. Kalidindi, P. Van Houtte, and E. Aernoudt: *Acta Mater.*, 2001, vol. 49, pp. 1607-19.
54. G.I. Taylor: *J. Inst. Met.*, 1938, vol. 62, pp. 307-24.
55. S.R. Kalidindi, C.A. Brokhorst, and L. Anand: *J. Mech. Phys. Solids*, 1992, vol. 40, pp. 537-69.
56. V. Bachu and S.R. Kalidindi: *Mater. Sci. Eng.*, 1998, vol. A257, pp. 108-17.
57. A. Bhattacharyya, E. El-Danaf, S.R. Kalidindi, and R.D. Doherty: *Int. J. Plasticity*, 2001, vol. 17, pp. 861-83.
58. A. Gholinia, P.B. Prangnell, and M.V. Markushev: *Acta Mater.*, 2000, vol. 48, pp. 1115-30.